Plane-symmetric cosmology with relativistic hydrodynamics

Peter Anninos

Laboratory for Computational Astrophysics, National Center for Supercomputing Applications,
University of Illinois at Urbana-Champaign, 405 North Mathews Avenue, Urbana, Illinois 61801

A numerical code, developed for cosmology and to investigate fully nonlinear behavior in the plane-symmetric Einstein equations, is described in detail. The field equations are solved self-consistently with the general relativistic hydrodynamical conservation equations, using artificial viscosity methods for shock capturing and an ideal fluid stress-energy tensor with a cosmological constant. Several tests of the code are presented, including anisotropically expanding vacuum and isotropically expanding de Sitter, dust-filled and radiation-filled cosmologies, gravitational waves in flat and anisotropically expanding background models, sub- and super-horizon scale density perturbations in an expanding FLRW background, and both Newtonian and relativistic shock tube evolutions. Also discussed is a gauge drift instability that can appear in near-geodesic evolutions of density perturbations when the dynamical time scale of collapse becomes smaller than the cosmological expansion rate. [S0556-2821(98)00918-7]

I. INTRODUCTION

Einstein's equations form a complex system of highly nonlinear hyperbolic and elliptic partial differential equations. For all the progress in recent years in finding solutions to the classical field equations, many basic issues regarding the nonlinear gravitational field and its cosmological consequences remain unresolved. Our understanding is complicated even further with the addition of matter sources and more elaborate models of the Universe. As general relativistic effects can play a significant role in astrophysical and cosmological processes it is important to account for nonlinear interactions between the gravitational field, matter sources, and the cosmological "background," especially in strong field regimes, over scales comparable to the horizon size, and at early epochs when cosmological models can be curvature dominated. For example, inflationary scalar fields [1,2], strong gravitational waves [3], element nucleosynthesis [4], and high order cosmic microwave background (CMB) anisotropies [5,6], are intrinsically nonlinear phenomenon and require full and self-consistent solutions to the Einstein equations. Moreover, a new generation of wave detectors are anticipated to observe gravitational waves before too long. Because waves will likely have originated in regions with highly dynamic and nonlinear gravitational fields, it is essential to study the strong as well as the weak field regimes, together with evolving matter structures in a cosmological framework.

The complexity of the coupled Einstein-matter system has motivated the development of a numerical code to solve the general equations without recourse to any simplifying linearized assumptions. Although the code is specialized to planar symmetry it can be used to simulate a wide range of physical conditions in inhomogeneous spacetimes containing an ideal gas or in vacuum. It is written in a general fashion and can easily be applied to expanding cosmological as well as asymptotically flat or Minkowski background spacetimes. This paper may be considered as the fourth in a "series" by Anninos, Centrella and Matzner [7,8,3], which were themselves motivated by the earlier work of Centrella and Wilson [9,10]. The first paper in the "series" [7] dealt exclusively with the initial value problem for vacuum plane-symmetric cosmologies, describing the numerical techniques and some nonlinear solutions to the momentum and Hamiltonian constraint equations. The second paper [8] focused on solving the vacuum evolution equations, while the third [3] applied this code to discuss the nonlinear propagation of gravitational waves in expanding universes. However, these results were limited to vacuum spacetimes and without the full dynamical degrees of freedom allowed by plane symmetry.

This work extends the capabilities of previous generation codes and the improvements are described here in detail. The major advances are the generalization to a non-diagonal metric, allowing for e_+ and $e_\times$ polarizations of gravity waves and a more general class of background cosmological models. (Because of the imposed symmetries, the previous work was limited to only e_+ wave states and the "degenerate" Kasner and flat space background models.) Also added are a cosmological constant, hydrodynamic fluid sources with robust shock capturing capability, and a more general set of slicing conditions that allow for asymptotically flat spacetimes as well as cosmologies with periodically identified boundaries. The code can be used for studies of Friedmann-Robertson-Lemaître-Walker (FLRW) models with arbitrarily large amplitude and long wavelength perturbations, large curvature anisotropies including generalized Kasner models, and strong field dynamics of gravitational wave, density or radiation dominated fluctuations.

Although this paper describes a general approach to solving the Einstein and relativistic hydrodynamics equations, it is worth pointing out an alternative approach that has proven especially convenient for plane symmetric cosmologies, and in particular the vacuum Gowdy models [11]. In this class of spacetimes, the Einstein equations decouple into dynamical equations for the wave amplitudes and easily solved constraints [11–13], which can be evolved using either conven-

tional time explicit schemes or a symplectic differential equation solver [14,15]. However, the methodology reported in this paper may be applied easily to more generic cosmological models, where it is not clear whether a convenient variable choice exists.

The remainder of this paper is organized as follows: Einstein's equations are written out in the $3+1$ or Arnowitt-Deser-Misner (ADM) form in Sec. II, together with the hydrodynamic conservation equations and gauge functions. A prescription for setting up initial data is described in Sec. III. The numerical methods, boundary conditions, gauge slicings, and choice of timesteps are summarized in Sec. IV. Several benchmark tests designed to confirm the robustness of the code for a wide variety of physical processes are presented in Sec. V, along with discussions of a gauge drift instability that can show up rather dramatically in evolutions of density perturbations. This work is summarized in Sec. VI.

II. BASIC EQUATIONS

The general spacetime metric can be written as

$$ds^2 = (-\alpha^2 + \beta_i \beta^i)dt^2 + 2\beta_i dx^i dt + \gamma_{ij} dx^i dx^j, \quad (1)$$

in the standard $3+1$ or ADM [16] formulation, where α and β^i are the lapse function and shift vector respectively, and γ_{ij} is the spatial 3-metric. The Einstein equations amount to four constraints,

$$^{(3)}R + K^2 - K_{ij}K^{ij} = 16\pi G\rho_H, \quad (2)$$

$$\nabla_i(K^{ij} - \gamma^{ij}K) = 8\pi G s^j, \quad (3)$$

twelve evolution equations,

$$\partial_t \gamma_{ij} = -2\alpha K_{ij} + \mathcal{L}_\beta \gamma_{ij}, \quad (4)$$

$$\partial_t K_{ij} = -\nabla_i \nabla_j \alpha$$
$$+ \alpha \left[{}^{(3)}R_{ij} - 2K_{ik}K_j^k + KK_{ij} \right.$$
$$\left. - 8\pi G \left(s_{ij} - \frac{1}{2}s\gamma_{ij} + \frac{1}{2}\rho_H \gamma_{ij} \right) \right] + \mathcal{L}_\beta K_{ij}, \quad (5)$$

and four kinematical or coordinate conditions for the lapse and shift vector that can be specified arbitrarily. Here,

$$\mathcal{L}_\beta \gamma_{ij} = \nabla_i \beta_j + \nabla_j \beta_i, \quad (6)$$

$$\mathcal{L}_\beta K_{ij} = \beta^k \nabla_k K_{ij} + K_{ik}\nabla_j \beta^k + K_{kj}\nabla_i \beta^k, \quad (7)$$

and ∇_i is the spatial covariant derivative with respect to γ_{ij}, ${}^{(3)}R_{ij}$ is the spatial Ricci tensor, K is the trace of the extrinsic curvature K_{ij}, G is the gravitational constant, and ρ_H, s^j, s and s_{ij} are the matter source terms as seen by observers at rest in the time slices. The units are such that $c = G = 1$, and the usual convention is adopted whereby greek (latin) indices refer to 4(3)-dimensional quantities.

The shift vector is set to zero, hence $\mathcal{L}_\beta \gamma_{ij} = \mathcal{L}_\beta K_{ij} = 0$. Several options are implemented for the lapse function, in-

cluding geodesic ($\alpha = 1$), algebraic, maximal, mean curvature, and harmonic slicing. The algebraic condition takes the form

$$\alpha = F(x^i)G(\gamma), \quad (8)$$

where $F(x^i)$ is an arbitrary function of the spatial coordinates specified at the initial time, and $G(\gamma)$ is a dynamic function of the determinant of the 3-metric. This condition has the advantage of simplicity and, for certain choices of G [i.e., those with the behavior $G(\gamma) \to 0$ as $\gamma \to 0$] also mimics maximal slicing in its singularity avoidance properties [17]. However, Eq. (8) can also be used for even more general (non-singularity avoiding) slicings to preserve, for example, the longitudinal gauge for cosmological perturbations as discussed in Sec. V D. The maximal slicing equation is derived by taking the trace of Eq. (5),

$$\nabla^i \nabla_i \alpha = \alpha[K_{ij}K^{ij} + 4\pi G(\rho_H + s)] + \beta^i \nabla_i K - \partial_t K, \quad (9)$$

and setting $K = \partial_t K = 0$. Mean curvature slicing also solves Eq. (9) but assumes $K = K(t)$, which can either be specified in advance or determined by imposing a boundary condition on the lapse function after solving Eq. (9) for the quantity $\alpha/\partial_t K$ [10,8]. This slicing condition is the most natural one for cosmology as it foliates homogeneous cosmological spacetimes with surfaces of homogeneity. The harmonic slicing condition is derived by imposing the harmonic condition on the time coordinate, leading to the evolution equation

$$\partial_t \alpha = -\alpha^2 K, \quad (10)$$

for which the initial value of the lapse is arbitrary.

The stress-energy tensor for an ideal fluid and a cosmological constant Λ is

$$T_{\mu\nu} = \rho h u_\mu u_\nu + P g_{\mu\nu} - \frac{\Lambda}{8\pi G} g_{\mu\nu}, \quad (11)$$

where $g_{\mu\nu}$ is the 4-metric, $h = 1 + \epsilon + P/\rho$ is the relativistic enthalpy of an ideal fluid, and ϵ, P, ρ and u_μ are the specific internal energy (per unit mass), pressure, rest mass density and four-velocity of the fluid. Defining

$$u = -n_\mu u^\mu = \alpha u^0 = (1 + u^i u_i)^{1/2}$$
$$= \left(1 - \frac{V_i V^i}{\alpha^2}\right)^{-1/2}, \quad (12)$$

as the generalization of the special relativistic Lorentz factor, the source terms in Eqs. (2)–(5) can be written in terms of the fluid variables as

$$\rho_H = n^\mu n^\nu T_{\mu\nu} = \rho h u^2 - P + \frac{\Lambda}{8\pi G}, \quad (13)$$

$$s_i = -\gamma_i^\mu n^\nu T_{\mu\nu} = \rho h u u_i, \quad (14)$$

$$s_{ij} = \gamma_i^\mu \gamma_j^\nu T_{\mu\nu} = \rho h u_i u_j + P\gamma_{ij} - \frac{\Lambda}{8\pi G}\gamma_{ij}, \quad (15)$$

with

$$s = s^i{}_i = 3P + \rho h(u^2 - 1) - \frac{3\Lambda}{8\pi G}, \tag{16}$$

and $n^\mu = (1, -\beta^i)/\alpha$ is the time-like normal congruence to the spatial hypersurfaces.

The hydrodynamics equations are derived from the normalization of the 4-velocity $u^\mu u_\mu = -1$, the conservation of baryon number $\nabla_\mu(\rho u^\mu) = 0$, the conservation of stress-energy $\nabla_\mu T^{\mu\nu} = 0$, and an equation of state $P = P(\rho, \epsilon)$, which for an ideal gas is $P = (\Gamma - 1)E/W = (\Gamma - 1)\rho\epsilon$, where Γ is the adiabatic index and W is defined below. The resulting equations can be written in flux conservative form as [18]

$$\frac{\partial D}{\partial t} + \frac{\partial(DV^i)}{\partial x^i} = 0, \tag{17}$$

$$\frac{\partial E}{\partial t} + \frac{\partial(EV^i)}{\partial x^i} + P\frac{\partial W}{\partial t} + P\frac{\partial(WV^i)}{\partial x^i} = 0, \tag{18}$$

$$\frac{\partial S_i}{\partial t} + \frac{\partial(S_i V^j)}{\partial x^j} - \frac{S^\mu S^\nu}{2S^0}\frac{\partial g_{\mu\nu}}{\partial x^i} + \sqrt{-g}\,\frac{\partial P}{\partial x^i} = 0, \tag{19}$$

where

$$W = \sqrt{-g}\,u^0, \tag{20}$$

$$D = W\rho, \tag{21}$$

$$E = W\rho\epsilon, \tag{22}$$

$$S_i = W\rho h u_i, \tag{23}$$

$$V^i = u^i/u^0, \tag{24}$$

and g is the determinant of the 4-metric. The system of Eqs. (17)–(24) are complimented by two additional expressions for V^i and W that are convenient for numerical computation. Defining

$$M = W\rho h = E + D + PW, \tag{25}$$

the momentum can be expressed as $S_\mu = Mu_\mu$, and S_0 is computed from the normalization of the four-velocity $S^\mu S_\mu = -M^2$. The coordinate velocity then becomes $V^i = S^i/S^0$ with $V^0 = 1$. Also, the time component of the four-velocity u^0 can be calculated from the normalization condition $u_\mu u^\mu = u^0 V^\mu S_\mu/M = -1$, and used to derive the following expression for W:

$$W = \frac{-\sqrt{|g|}M}{S_\mu V^\mu}. \tag{26}$$

All of the above equations are valid for general, multi-dimensional, vacuum and ideal fluid spacetimes. However, the work presented in this paper is specialized to plane symmetry and all variables are functions only of one spatial dimension (taken to be the z-axis) and time, with a spatial 3-metric

$$\gamma_{ij} = \begin{pmatrix} \gamma_{xx} & \gamma_{xy} & 0 \\ \gamma_{xy} & \gamma_{yy} & 0 \\ 0 & 0 & \gamma_{zz} \end{pmatrix}, \tag{27}$$

and extrinsic curvature

$$K_{ij} = \begin{pmatrix} K_{xx} & K_{xy} & 0 \\ K_{xy} & K_{yy} & 0 \\ 0 & 0 & K_{zz} \end{pmatrix}. \tag{28}$$

The metric (27) generalizes previous treatments [9,10,7,8,3] of plane-symmetric spacetimes by including a nondiagonal component to model both polarization states of gravitational waves. This more general metric also accommodates a broader range of background anisotropic cosmological models, as each of the nonvanishing components can be initialized and evolved without restrictions but for the Hamiltonian and momentum constraints.

III. INITIAL DATA

The constraint equations (2) and (3) are solved using York's [19] conformal prescription to obtain proper initial data for evolution. The method introduces a conformal transformation of the 3-metric $\gamma_{ij} = \phi^4\hat{\gamma}_{ij}$, trace-free momentum components $A^{ij} = K^{ij} - \gamma^{ij}K/3 = \phi^{-10}\hat{A}^{ij}$, and matter source terms $s^i = \phi^{-10}\hat{s}^i$ and $\rho_H = \phi^{-n}\hat{\rho}_H$, where $n > 5$ for uniqueness of solutions to the elliptic equation (29) below [19]. Further decomposing the free momentum variables into transverse and longitudinal components $\hat{A}^{ij} = \hat{A}^{ij}_* + (\hat{l}w)^{ij}$, the Hamiltonian and momentum constraints can be written as

$$\hat{\nabla}_i\hat{\nabla}^i\phi - \frac{\hat{R}}{8}\phi + \frac{1}{8}\hat{A}_{ij}\hat{A}^{ij}\phi^{-7} - \frac{1}{12}K^2\phi^5 + 2\pi G\hat{\rho}_H\phi^{5-n} = 0, \tag{29}$$

$$(\hat{\nabla}_j\hat{\nabla}^j w)^i + \frac{1}{3}\hat{\nabla}^i(\hat{\nabla}_j w^j) + \hat{R}^i_j w^j - \frac{2}{3}\phi^6\hat{\nabla}^i K - 8\pi G\hat{s}^i = 0, \tag{30}$$

where the longitudinal part of $\hat{A}^{ij}$ is

$$(\hat{l}w)^{ij} = \hat{\nabla}^i w^j + \hat{\nabla}^j w^i - \frac{2}{3}\hat{\gamma}^{ij}\hat{\nabla}_k w^k, \tag{31}$$

and the transverse part satisfies $\hat{\nabla}_j\hat{A}^{ij}_* = \hat{A}^j_{*j} = 0$. Also, $\hat{\nabla}_i$ is the spatial covariant derivative evaluated with the conformal 3-metric $\hat{\gamma}_{ij}$, $\hat{R}_{ij}$ is the corresponding conformal Ricci tensor and $\hat{R} = \hat{\gamma}^{ij}\hat{R}_{ij}$ is its trace. Equations (29) and (30), which form a coupled nonlinear set of elliptic equations, are solved using an iterative procedure. The two equations can, however, be decoupled if either a maximal ($K = \partial_t K = 0$) or mean curvature [$K = K(t)$] slicing condition is assumed.

An additional complication is introduced by the hydrodynamic variables due to the intrinsic coupling through the boost factor (12). Neglecting the cosmological constant, the conformal form of Eq. (13) can be expanded as

$$\hat{\rho}_H = \hat{\rho}\hat{u}^2 + (\hat{e} + \hat{P})\hat{u}^2 - \hat{P}, \tag{32}$$

where $e = \rho\epsilon$. In order to provide some control over the initial hydrodynamic data, and to easily reconstruct the physical variables, the condition $u^2 = \hat{u}^2$ is imposed, where

$$u^2 = 1 + \frac{S_i S^i}{(D+E+PW)^2}$$

$$= 1 + \frac{s_i s^i}{u^2(\rho+e+P)^2}. \tag{33}$$

This condition is satisfied for an ideal gas with $P = (\Gamma - 1)e$ and the same conformal scaling of the density and internal energy, $\rho = \phi^{-8}\hat{\rho}$ and $e = \phi^{-8}\hat{e}$, i.e. $n = 8$ in Eq. (29). In cases where $s^i = 0$, and for an ideal gas in which $P \propto e \propto \rho^{\Gamma}$, the condition $u^2 = \hat{u}^2$ can still be maintained by setting $\rho = \phi^{-n}\hat{\rho}$ and $e = \phi^{-\Gamma n}\hat{e}$ with $n > 5$ (but arbitrary otherwise) to preserve motion along a constant adiabat for shock-free flows [20].

In formulating a parametric procedure to solve the initial value problem, two basic situations are considered: $s^i = 0$ and $s^i \neq 0$. In the former case, the longitudinal part of the momentum data can be set to zero assuming that K is also homogeneous. It is then only necessary to enforce the transverse and trace-free (TT) conditions, $\hat{\nabla}_j \hat{A}_*^{ij} = \hat{A}_{*i}^i = 0$. For the

cases in which $s^i \neq 0$, a flat space conformal metric ($\hat{\gamma}_{ij} = \delta_{ij}$) is assumed so that the momentum constraint (30) reduces to

$$\frac{\partial^2 w^z}{\partial z^2} = 6\pi G\hat{s}^z + \frac{\phi^6}{2}\frac{\partial K}{\partial z}, \tag{34}$$

for one-dimensional perturbations along the z axis, and

$$(\hat{l}w)^{ij} = \begin{pmatrix} -\frac{2}{3}\partial_z w^z & 0 & 0 \\ 0 & -\frac{2}{3}\partial_z w^z & 0 \\ 0 & 0 & \frac{4}{3}\partial_z w^z \end{pmatrix}. \tag{35}$$

Additional free elements can be added to the transverse momenta by noting that

$$\hat{A}_*^{xx} = a_1(t) - f(t,z), \tag{36}$$

$$\hat{A}_*^{yy} = a_2(t) + f(t,z), \tag{37}$$

$$\hat{A}_*^{zz} = -a_1(t) - a_2(t), \tag{38}$$

$$\hat{A}_*^{xy} = g(t,z) \tag{39}$$

satisfy the TT conditions for arbitrary a_1, a_2, f and g, provided $\hat{\gamma}_{ij} = \delta_{ij}$ (although equivalent expressions can be derived for nonflat conformal metrics). The general free momenta data then become

$$\hat{A}^{ij} = \begin{pmatrix} a_1(t) - f(t,z) - \frac{2}{3}\partial_z w^z(t,z) & g(t,z) & 0 \\ g(t,z) & a_2(t) + f(t,z) - \frac{2}{3}\partial_z w^z(t,z) & 0 \\ 0 & 0 & -a_1(t) - a_2(t) + \frac{4}{3}\partial_z w^z(t,z) \end{pmatrix}. \tag{40}$$

For conformally flat backgrounds (e.g. the FLRW solutions), the trace-free momenta are zero and these classes of spacetimes can be initialized simply by setting $a_1 = a_2 = 0$. Anisotropic background spacetimes (e.g. the Kasner solutions) can also be modeled by a proper choice of the conformal metric and transverse momentum functions a_1 and a_2, as shown in Table I. Furthermore, cosmological perturbations can be set up in the convenient longitudinal (or conformal-Newtonian) gauge using the York procedure by defining the free data as $\hat{\gamma}_{ij} = \delta_{ij}$, $\hat{A}^{ij} = 0$, and specifying ρ, s^i, α, and K with Eqs. (67), (68), (69), and (70) respectively.

After choosing $\hat{A}_*^{ij}$ from Eqs. (36)–(39), and solving Eqs. (34) and (35) for $(\hat{l}w)^{ij}$, $\hat{A}^{ij}$ is reconstructed from Eq. (40), and the conformal factor ϕ from Eq. (29). The initial value problem is completed by iterating the process until the solu-

tion for ϕ converges to one part in 10^{10}. The initial data is thus parametrized by the homogeneous background parameters (a_1 and a_2) and the scalar (ϕ or ρ) and tensor (f and g) mode functions. The form of $\hat{A}_*^{ij}$, together with a flat conformal metric, suggests that the tensor mode perturbations are a superposition of leftward and rightward traveling waves, which are initially exactly out of phase.

An important cosmological length scale that should be considered when setting up initial data is the particle horizon size (in comoving coordinates) along the axis of inhomogeneity, which is approximated by

$$L_H = \int_0^t \frac{dt}{\sqrt{\gamma_{zz}}} = \frac{t}{1-p_3}\frac{1}{\sqrt{\gamma_{zz}}} \quad \text{or} \quad \frac{2}{H_0}\sqrt{a}. \tag{41}$$

TABLE I. Solutions to four different classes of homogeneously expanding spacetimes. Λ, ρ, e, K, γ_{ij} and A^{ij} are the cosmological constant, fluid density, fluid internal energy (per unit volume), trace of extrinsic curvature tensor, spatial 3-metric, and the trace-free momentum tensor. In all cases, a diagonal metric and unit lapse are assumed. The anisotropy parameters in the Kasner solutions satisfy the conditions $\Sigma_i p_i = \Sigma_i p_i^2 = 1$ arising from the Hamiltonian constraint.

Spacetime	Λ	ρ	e	K	γ_{ij} ($i=j$)	A^{ij} ($i=j$)
de Sitter	Λ	0	0	$-\sqrt{3\Lambda}$	$e^{\sqrt{4\Lambda/3}t}$	0
Kasner	0	0	0	$-1/t$	$(t/t_0)^{2p_i}$	$\left(\dfrac{t_0}{t}\right)^{2p_i+1}\left(\dfrac{1-3p_i}{3t_0}\right)$
FLRW/dust	0	$1/(6\pi Gt^2)$	0	$-2/t$	$(t/t_0)^{4/3}$	0
FLRW/radiation	0	0	$3/(32\pi Gt^2)$	$-3/(2t)$	t/t_0	0

The above result is valid for a metric component $\gamma_{zz}\propto t^{2p_3}$ in the anisotropic models, or $\gamma_{zz}=a(t)^2\propto t^{4/3}$ with a present day Hubble parameter H_0 in the dust-filled FLRW spacetimes. The significance of this scale is particularly evident in the Kasner wave (64) and FLRW density (67) solutions. For perturbation wavelengths $\lambda \gg L_H$, the density and metric fluctuations remain essentially constant. For $\lambda \ll L_H$, the oscillatory behavior of plane waves is recovered, as is the Zel'dovich [21] solution in which the matter perturbations grow as $\delta\rho/\rho\propto a$.

A second important scale parameter, say for a baryonic fluid composed of hydrogen gas, is the Jeans mass

$$M_J=\left(\frac{\pi k_B\Gamma T_K}{m_pG}\right)^{3/2}\rho^{-1/2}, \tag{42}$$

where k_B, m_p, and T_K are the Boltzmann's constant, proton mass, and gas temperature in degrees kelvin. The corresponding comoving Jeans length $L_J\equiv(M_J/\rho_c)^{1/3}$, where ρ_c represents the average density in comoving coordinates, dictates the scale at which pressure forces balance the self-gravity. It is convenient to combine the two length scales into a single dimensionless parameter

$$\frac{L_J}{L_H}\approx(\Gamma T_K)^{1/2}\times 10^{-6}, \tag{43}$$

where the background cosmological density for the flat FLRW model $\rho=\rho_0=3H_0^2/8\pi Ga^3$ is assumed in Eq. (42). As an example, consider a baryonic fluid in the observed or post-recombination Universe. At sufficiently early times (redshifts greater than around 100), the fluid is coupled to the cosmic microwave background radiation (CMBR) so that $T\propto(1+z)$ and $L_J/L_H\sim(1+z)^{1/2}\times10^{-6}$, where here z represents the cosmological redshift. At smaller redshifts, the gas recombines and decouples from the photon field to cool adiabatically $T\propto(1+z)^{3(\Gamma-1)}$, resulting in $L_J/L_H\sim(1+z)\times10^{-7}$ for a monotonic ideal gas with adiabatic index $\Gamma=5/3$. In any case, a pressure-free solution is a good approximation for the baryons in the observed cosmological perturbative regime at scales $\lambda\gg10^{-5}L_H$.

IV. NUMERICAL METHODS

The z axis is discretized with uniform grid spacing and the evolved variables are centered either at the zone edges (the velocity V^z and momentum S_z vectors) or zone centers (all other scalar or tensor variables). Periodic, specified and flat (vanishing first derivative) boundary conditions are supported in the evolutions. A two-step Lax-Wendroff scheme [22] that is second order accurate in time and space is implemented to integrate the Einstein equations (4),(5) and the harmonic lapse equation (10), using a variable timestep procedure. Although the Lax-Wendroff method is generally more diffusive than the standard leapfrog used in references [8,3] and typically requires slightly greater grid resolution to achieve comparable accuracy (as measured by the damping and dispersion rates of gravitational waves), this is more than offset by the convenience of maintaining all the variables at the same time levels since increasing grid resolution is not an issue in plane symmetry if the code is convergent. Furthermore, the Lax-Wendroff scheme is likely to be more stable for problems involving strong field gradients. The hydrodynamic equations (17)–(19) are solved with time-explicit methods together with operator splitting, artificial viscosity for shock capturing [10,23], second order van Leer monotonic interpolation [24], and an option for consistent transport [25]. The numerical methods are not discussed here in any great detail since they can be found in the indicated references. However, the order in which the various source terms are updated can affect the numerical accuracy. The following order has been determined to produce the desired convergence rate, assuming an appropriate initial data set has already been specified:

Compute timestep Δt from Eq. (46),

Evolve γ_{ij} using Eq. (4),

Compute components of the Ricci tensor $^{(3)}R_{ij}$,

Evolve K_{ij} using Eq. (5) as a single source update,

Solve for K either by $K^{n+1}=K^n+\Delta t\dot{K}$ for mean curvature slicing, setting $K=0$ for maximal slicing, or more generally constructing K from the trace of the evolved K_{ij},

Evolve hydrodynamic variables:

Normalize velocity $V^z=S^z/S^0$ using $S_\mu S^\mu=-M^2$ and Eq. (25),

Solve for the relativistic boost factor W from Eq. (26),

Compute artificial viscosity $Q=Q_{av}(D+E+PW)(\Delta V^z)^2$,

where Q_{av} is a constant typically equal to 3 for the approximate number of zones used to capture shocks,

Update S_z in Eq. (19), accounting for the gravitational acceleration terms,

Update S_z in Eq. (19), accounting for the pressure acceleration and viscosity terms,

Update E in Eq. (18), accounting for the compressional heating, $\dot{W}$ and artificial viscosity terms,

Update D, E and S_z in Eqs. (17), (18) and (19), accounting for the transport terms,

Construct the ADM matter source terms ρ_H, s^j, s_{ij} and s from Eqs. (13)–(16).

Solve for the lapse function either by setting $\alpha=1$ for geodesic slicing, evolving Eq. (10) for harmonic slicing, or solving Eq. (9) for maximal slicing (with $\dot{K}=0$) or for a more general specified slicing condition, i.e. mean curvature with $K(t)$. Mean curvature slicing can be applied either by specifying $\dot{K}$ beforehand, or by allowing the evolution to determine $\dot{K}$ by imposing a boundary condition on α such that $\alpha=1$ at the grid edges [10,8].

The above sequence is repeated twice in the two-step Lax-Wendroff scheme, which is written schematically for the metric evolution equations as

$$\gamma_i^{n+1/2}=\frac{1}{2}(\gamma_{i-1}^n+\gamma_{i+1}^n)-2\alpha_i^n K_i^n\left(\frac{\Delta t}{2}\right), \qquad (44)$$

$$\gamma_i^{n+1}=\gamma_i^n-2\alpha_i^{n+1/2}K_i^{n+1/2}(\Delta t), \qquad (45)$$

where the tensor index notation has been dropped here, so that subscripts label the spatial zones and superscripts indicate the temporal levels.

Although the evolved data are not constrained to satisfy either the momentum or Hamiltonian equations (except initially), the residuals of Eqs. (2) and (3) are evaluated during the evolutions to verify the accuracy of solutions and to confirm the proper convergence behavior. In solving the elliptic equations for the Hamiltonian constraint and lapse function, the differential equations are discretized to form an $N \times N$ matrix of equations, where N is the number of zones along the z axis. The resulting algebraic equations are solved using a tridiagonal algorithm in the case of Dirichlet boundary conditions. For periodic boundary conditions, a variant of the tridiagonal algorithm [8] is implemented to introduce an additional pass through the matrix solve and eliminate the corner elements arising from periodicity.

The timestep is defined as the minimum constraint arising from considerations of the light speed, sound speed, fluid velocity, cosmological expansion rate, and the magnitude of the artificial viscosity coefficient to maintain stability in shock flows. Since the timesteps can be nonuniform, an additional constraint is placed so that Δt does not vary by more than 10% per timestep. In summary,

$$\Delta t=\min\left\{\frac{C_{lt}\Delta z\sqrt{g_{zz}}}{\alpha},\frac{C_{ex}}{\alpha K},\frac{C_{ex}K}{\dot{K}},\right.$$

$$\left.\frac{C_{cs}\Delta z}{\sqrt{\Gamma P/\rho}},\frac{C_{cs}\Delta z}{V^z},\frac{C_{cs}\Delta z}{4Q_{av}\Delta V},1.1\times\Delta t_{old}\right\}, \qquad (46)$$

where $\alpha K=-\partial_t(\sqrt{\gamma})/\sqrt{\gamma}$ is a measure of the relative rate of change of the 3-volume element, and the expression $C_{ex}K/\dot{K}$ is used in place of $C_{ex}/\alpha K$ for the expansion constraint if the spacetime is foliated by mean curvature slicings. The coefficients C_{lt}, C_{ex} and C_{cs} are constants representing the light speed, expansion, and sound speed Courant factors. Typical values are $C_{lt}=0.05$, $C_{ex}=0.005$ and $C_{cs}=0.4$.

V. CODE TESTS

Several benchmark tests of the code are presented in this section. The various tests are chosen to calibrate the code's performance on a number of different physical problems, including evolutions of isotropically and anisotropically expanding universes, shock generating fluid flows, gravitational waves in flat and expanding backgrounds, and cosmological matter perturbations. The convergent nature of the results is stressed in each case.

A. Homogeneous cosmologies

Assuming a diagonal metric of the form

$$ds^2=-dt^2+A(t)dx^2+B(t)dy^2+C(t)dz^2, \qquad (47)$$

and setting the spatial derivatives to zero and the coordinate and fluid flow lines normal to the spatial hypersurfaces, the homogeneous, but anisotropic, Einstein equations reduce to

$$\frac{\ddot{A}}{A}=\frac{\dot{A}^2}{2A^2}-\frac{\dot{A}\dot{B}}{2AB}-\frac{\dot{A}\dot{C}}{2AC}+8\pi G(\rho+e-P)+2\Lambda, \qquad (48)$$

$$\frac{\ddot{B}}{B}=\frac{\dot{B}^2}{2B^2}-\frac{\dot{A}\dot{B}}{2AB}-\frac{\dot{B}\dot{C}}{2BC}+8\pi G(\rho+e-P)+2\Lambda, \qquad (49)$$

$$\frac{\ddot{C}}{C}=\frac{\dot{C}^2}{2C^2}-\frac{\dot{A}\dot{C}}{2AC}-\frac{\dot{B}\dot{C}}{2BC}+8\pi G(\rho+e-P)+2\Lambda, \qquad (50)$$

where dots indicate time derivatives. Additional equations are provided by the Hamiltonian constraint (or first integral)

$$\frac{\dot{A}\dot{B}}{AB}+\frac{\dot{A}\dot{C}}{AC}+\frac{\dot{B}\dot{C}}{BC}=32\pi G(\rho+e)+4\Lambda, \qquad (51)$$

and the mean curvature slicing condition (with $\alpha=1$)

$$\dot{K}=\frac{\dot{A}^2}{4A^2}+\frac{\dot{B}^2}{4B^2}+\frac{\dot{D}^2}{4D^2}+4\pi G(\rho+e+3P)-\Lambda. \qquad (52)$$

Also,

$$\rho=\rho_0(ABC)^{-1/2}, \qquad (53)$$

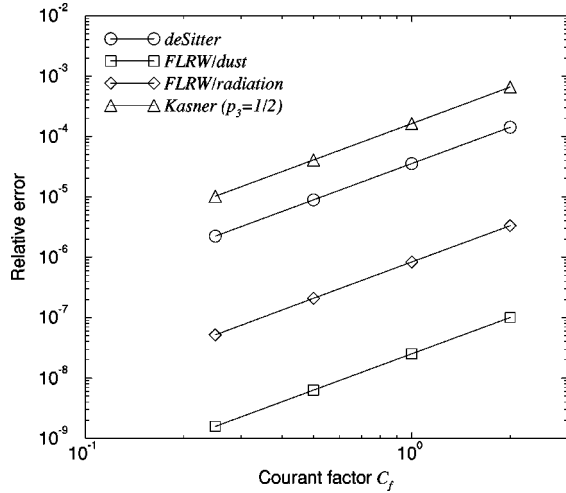$$e=e_0W^{-\Gamma}=e_0(ABC)^{-\Gamma/2} \qquad (54)$$

FIG. 1. Results from convergence studies of four different homogeneous spacetimes: isotropic exponentially expanding de Sitter, isotropic dust-driven FLRW, isotropic radiation-driven FLRW, and anisotropic Kasner (with $p_3 = 1/2$). The absolute relative errors, |numerical-analytic|/analytic, are plotted as a function of the Courant factor C_f defined in the text. The numerical solutions converge as expected with a scaling $(\Delta t)^2$.

are solutions to the mass and energy conservation equations (17) and (18) with constants of integration ρ_0 and e_0.

The following four spacetimes are considered: exponentially expanding deSitter cosmology with $\Lambda \neq 0$ and $\rho = e = 0$; anisotropic vacuum Kasner spacetime with $p_3 = 1/2$ and $\Lambda = \rho = e = 0$; dust dominated FLRW model with $\Lambda = e = 0$ and $\rho \neq 0$; and radiation dominated FLRW model with $\Lambda = \rho = 0$ and $P = e/3 \neq 0$. The various analytic solutions are summarized in Table I. The absolute relative errors between the numerical and analytic solutions, ie. |numerical-analytic|/ analytic, are plotted in Fig. 1 for each model as a function of the Courant factor C_f, defined as $\Delta t = C_f \times (C_{ex}, C_{lt})$, and $C_{ex} = 0.005$ and $C_{lt} = 0.05$ are the expansion and light speed coefficients mentioned in Sec. IV. The errors are calculated at times $t = 30t_0$, $t = 10^6 t_0$, $t = 10^6 t_0$, and $t = 10^4 t_0$, where $t_0 = 1$ is the initial time, corresponding to fractional changes in proper length scales of roughly e^{10}, 10^4, 10^3 and 10^2 along the z axis for the de Sitter, dust FLRW, radiation FLRW, and ($p_3 = 1/2$) Kasner tests respectively. As expected, the errors scale to second convergent order $(\Delta t)^2$.

B. Shock tube

To test the shock capturing algorithms and the ability of the code to evolve a rarefaction wave, two shock tube problems are considered: one Newtonian, the other special relativistic. In these problems, a (hot, cold) gas is set up to the (left, right) with no initial bulk fluid motion. The partition separating the two gases is removed at $t = t_0 = 1$. The head of the rarefaction wave then propagates into the denser gas at the local sound speed and a compression wave travels into the lower density gas, forming a shock front. This problem tests the ability of the code to evolve the three dynamical components of the gas: the rarefaction wave, the contact discontinuity, and the shock.
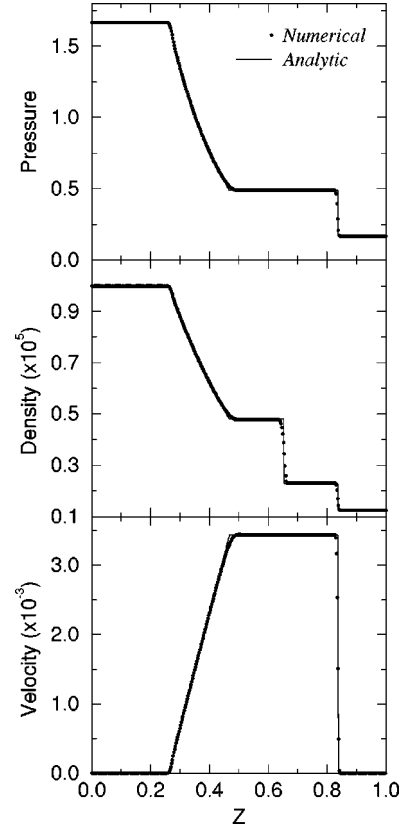

FIG. 2. Comparison of the Newtonian shock tube evolution (filled circles) with the analytic solution (solid lines). The initial data is $e = (2.5, 0.25)$ and $\rho = (10^5, 0.125 \times 10^5)$ for the (left, right) states. The adiabatic index is $\Gamma = 5/3$, the artificial viscosity constant is $Q_{av} = 3$, and the grid is resolved with 400 zones.

The initial data for the Newtonian case is $e = (2.5, 0.25)$ and $\rho = (10^5, 0.125 \times 10^5)$, and for the relativistic case $e = (20, 10^{-7})$ and $\rho = (10, 1)$, where the two numbers specified for each variable refer to the left and right states respectively. In both calculations, the adiabatic index is $\Gamma = 5/3$, the artificial viscosity coefficient is $Q_{av} = 3$, and the grid size is set to unity and resolved by 400 zones. The relatively large densities in the Newtonian case are required to set up a thermodynamically nonrelativistic flow such that $e/\rho = \epsilon \ll c^2$, where c is the unit light speed. The Newtonian calculation, shown in Fig. 2, results in maximum errors of 0.6%, 0.1% and 0.3% for the density, velocity and pressure respectively. For the relativistic calculation in Fig. 3, maximum errors of 17%, 1.4% and 5.9% are found in the density, velocity and pressure. Increasing the artificial viscosity constant improves the agreement at the shock front, especially in the more relativistic flows as considered here. [The maximum velocity in Fig. 3 reaches $V^z/c = 0.72$, corresponding to a Lorentz boost factor of $W = (1 - V^2)^{-1/2} = 1.44$.] In this case, a value of $Q_{av} = 10$ reduces the differences across the shock front by roughly 50% in the density.

C. Gravitational waves

1. Minkowski background

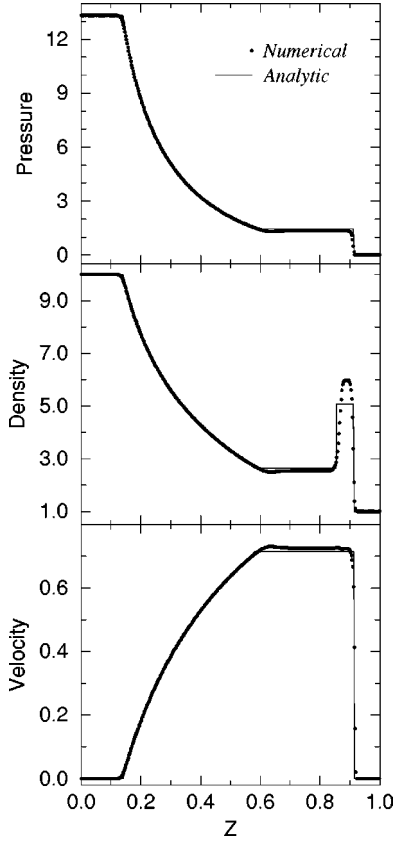Gravitational wave perturbations with both polarizations are expressed in the flat background and TT gauge as

FIG. 3. Comparison of the relativistic shock tube evolution (filled circles) with the analytic solution (solid lines). The initial data is $e=(20,10^{-7})$ and $\rho=(10,1)$ for the (left, right) states. The adiabatic index is $\Gamma=5/3$, the artificial viscosity constant is $Q_{av}=3$, and the grid is resolved with 400 zones. The maximum fluid velocity $V^z/c=0.72$ corresponds to a relativistic Lorentz factor of $W=1.44$.

$$\gamma_{ij}=\begin{pmatrix} 1-f & g & 0 \\ g & 1+f & 0 \\ 0 & 0 & 1 \end{pmatrix}, \qquad (55)$$

where f and g are functions of the wave-like coordinates $z\pm t$, and much smaller than unity. To linear order in f and g, $K=0$ and the trace-free momenta become

$$A^{ij}=-\frac{1}{2\alpha}\begin{pmatrix} -\dot{f} & \dot{g} & 0 \\ \dot{g} & \dot{f} & 0 \\ 0 & 0 & 0 \end{pmatrix}. \qquad (56)$$

The code tests are performed with two different data sets:

$$f=f_1\ \sin\!\left(\frac{2\pi}{L}(z-t+t_0)\right)$$

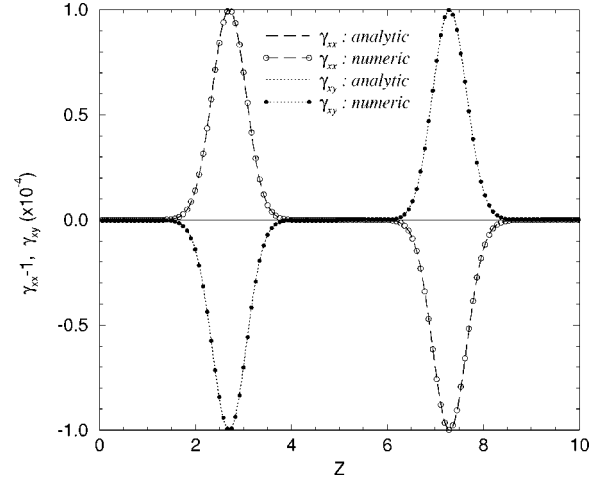$$-f_1\ \sin\!\left(\frac{2\pi}{L}(z+t-t_0)\right), \qquad (57)$$

FIG. 4. Spatial profiles of linear gravitational pulse waves with both polarizations. The initial data (solid line) consists of two oppositely traveling Gaussian pulses with amplitude $\pm 10^{-4}$, centered at the middle of the grid where they exactly cancel themselves out. The final solutions for $-f$ (open circles) and g (filled circles) are shown at time $t=3.3t_0$, where $t_0=1$ is the initial time, along with the corresponding analytic solutions (dashed and dotted lines).

$$g=g_1\ \sin\!\left(\frac{2\pi}{L}(z-t+t_0)\right)$$

$$-g_1\ \sin\!\left(\frac{2\pi}{L}(z+t-t_0)\right), \qquad (58)$$

with grid size $L=1$, and

$$f=f_1 e^{-(z-z_c-t+t_0)^2/\sigma^2}-f_1 e^{-(z-z_c+t-t_0)^2/\sigma^2}, \qquad (59)$$

$$g=g_1 e^{-(z-z_c-t+t_0)^2/\sigma^2}-g_1 e^{-(z-z_c+t-t_0)^2/\sigma^2}, \qquad (60)$$

with grid size $L=10$, pulse width $\sigma=0.05L$, and initial centered position $z_c=L/2$. Both tests have wave amplitudes $f_1=g_1=10^{-4}$ and are run to a final time $t_f=3.3t_0$. The first data set represents a standing wave solution, and the second is composed of two oppositely traveling Gaussian pulses with equal amplitudes but opposite signs.

Figure 4 shows the Gaussian pulse results at the initial $t_0=1$ (solid line) and final $t=3.3t_0$ (filled and open circles) times, comparing to the corresponding analytic solutions (dotted and dashed lines). At the final time plotted, the pulses have moved outward from the center of the grid where they were located at $t=t_0$ and had exactly canceled to a flat initial metric. Figure 5 shows the relative errors (as a function of grid resolution) in f and g for both data sets. The errors scale with $(\Delta t)^2$ and $(\Delta z)^2$ as expected.

2. Kasner background

A prescription for setting up initial wave data in a general anisotropic background was described in Sec. III. Considered here are perturbations of an anisotropic Kasner model [26]
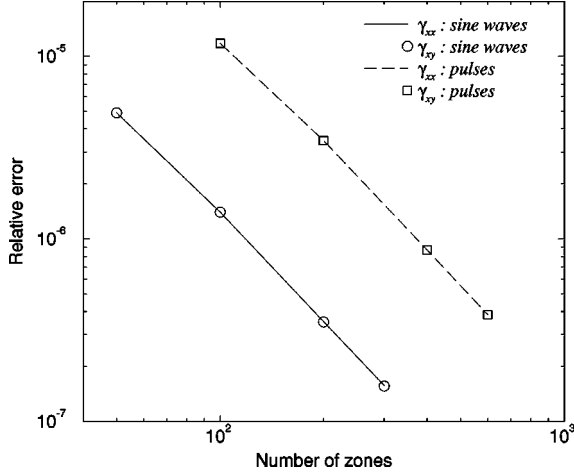
FIG. 5. Convergence study of the errors found in evolving linearized gravity waves of both polarization states. Results from two different data sets are shown: sinusoidal standing waves and oppositely traveling Gaussian pulses. Both initial data sets are defined with wave amplitudes of 10^{-4}. The errors are computed at time $t = 3.3 t_0$, where $t_0 = 1$ is the initial time, and scale as $(\Delta t)^2$ and $(\Delta z)^2$.

$$ds^2 = -dt^2 + \left(\frac{t}{t_0}\right)^{2p_1} dx^2 + \left(\frac{t}{t_0}\right)^{2p_2} dy^2 + \left(\frac{t}{t_0}\right)^{2p_3} dz^2, \tag{61}$$

where t_0 is an arbitrary scaling constant and the exponents p_i are subject to the constraints $p_1 + p_2 + p_3 = p_1^2 + p_2^2 + p_3^2 = 1$. In this case, the inhomogeneous metric can be written in a form analogous to Eq. (55)

$$ds^2 = -dt^2 + t^{4/3}(1 + f_1)dx^2$$
$$+ t^{4/3}(1 - f_1)dy^2 + t^{-2/3}dz^2, \tag{62}$$

where the specific choice $p_1 = p_2 = 2/3$ and $p_3 = -1/3$ has been made for the exponents and $f_1(t,z)$ is a perturbation function representing e_+ polarized waves propagating along the z axis. Assuming a spatial dependence of the form $f_1 = f(t)\sin(kz)$, the Einstein equations reduce to

$$\frac{d^2 f}{dt^2} + \frac{1}{t}\frac{df}{dt} + t^{2/3}k^2 f = 0, \tag{63}$$

with solution

$$f_1 = f_1^{(0)} J_0\left(\frac{3}{4}kt^{4/3}\right)\sin(kz), \tag{64}$$

where $f_1^{(0)}$ is a constant and $J_0(x)$ is the Bessel function of order zero. In the short wavelength limit, Eq. (64) reduces to

$$f_1 = f_1^{(0)}\sqrt{\frac{8}{3\pi k}}\left(\frac{1}{t}\right)^{2/3}\cos\left(\frac{3}{4}kt^{4/3} - \frac{\pi}{4}\right)\sin(kz), \tag{65}$$

and the solution decays like $t^{-2/3}$ as the background model expands.
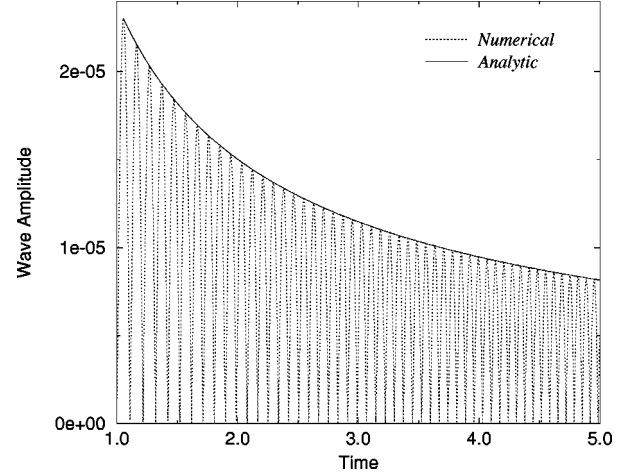

FIG. 6. The maximum value of $|\gamma_{xx} - \bar{\gamma}_{xx}|/\bar{\gamma}_{xx}$, where $\bar{\gamma}_{xx}$ is the average background value, is plotted as a function of time for gravitational waves traveling through the Kasner model with $p_1 = p_2 = 2/3$ and $p_3 = -1/3$. The absolute value of the wave amplitude, shown to 25 oscillation periods, decays as predicted by the analytic result $t^{-2/3}$ (solid line).

For the code test, the wave number is set to $k = 2\pi/L$ and the grid length L to one-third of the horizon size, using 100 zones to resolve the domain. The rate of decay found in the numerical calculations is compared to the analytic prediction in Fig. 6, where the quantity $|\gamma_{xx} - \bar{\gamma}_{xx}|/\bar{\gamma}_{xx}$ is plotted for the perturbation amplitude, and $\bar{\gamma}_{xx}$ is the homogeneous background value. The numerical and analytic results agree nicely in both the amplitude and oscillation frequencies.

D. Cosmological density perturbations

The metric for pressure-free density perturbations in an expanding flat universe is written in the longitudinal gauge as [27]

$$ds^2 = -(1 + 2\Phi)dt^2 + a^2(1 - 2\Phi)\delta_{ij}dx^i dx^j, \tag{66}$$

where $a = (3H_0 t/2)^{2/3}$ is the cosmological scale factor, H_0 is the present-day Hubble constant, $\Phi(z)$ is a time independent (for the growing modes) function defining the Newtonian gravitational potential,

$$\rho = \rho_0\left(1 + \frac{2a}{3H_0^2}\nabla_z^2\Phi - 2\Phi\right), \tag{67}$$

$$s^z = \frac{\gamma^{zz}S_z}{\sqrt{\gamma}} = -\frac{H_0}{4\pi G}a^{-7/2}\nabla_z\Phi = -\frac{1}{12\pi G}\gamma^{zz}\nabla_z K, \tag{68}$$

are the matter density and momentum respectively, and $\rho_0 = 3H_0^2/(8\pi G a^3)$ is the background average density. The implied slicing condition

$$\alpha = 1 + \Phi, \tag{69}$$
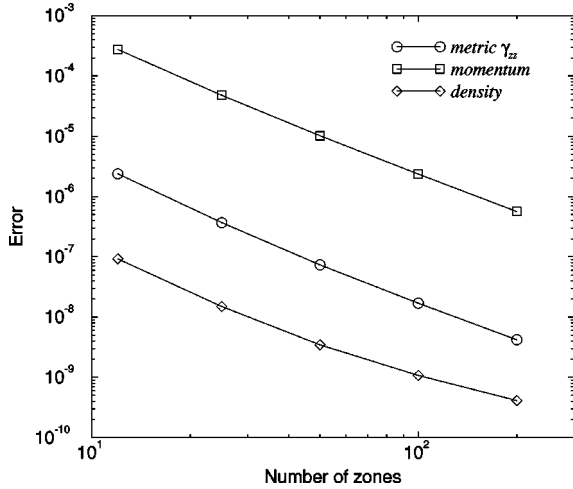
$$K = -3H_0 a^{-3/2}(1 - \Phi), \tag{70}$$

FIG. 7. Convergence study of the errors found in evolving super-horizon scale perturbations in the flat density dominated FLRW model. The initial data is a sine wave perturbation with amplitude 10^{-5} in the gravitational potential and comoving wavelength $\lambda = 10^3 L_H$, where L_H is the horizon length. The errors are computed at time $t = 10^6 t_0$ after the universe has expanded a factor of 10^4 along the z axis and $L/L_H \sim 10$. The displayed errors are the relative normalized differences for γ_{zz} and D, and the absolute differences in S_z. The errors scale as $(\Delta t)^2$ and $(\Delta z)^2$.
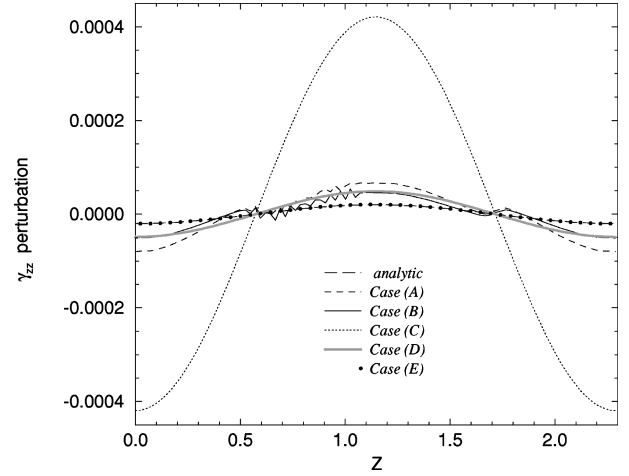

FIG. 8. Results from five different simulations of sub-horizon scale perturbations in the flat density dominated FLRW model. The initial data is a sine wave perturbation with an amplitude 10^{-5} in the gravitational potential and a comoving wavelength $\lambda = L_H$ which is resolved with 100 zones. The solutions for $(\gamma_{zz} - \bar{\gamma}_{zz})/\bar{\gamma}_{zz}$ are shown at time $t = 10^3 t_0$ when $L/L_H \sim 10^{-1}$. The evolutions are unstable for cases (A) and (B) in which the lapse function is fixed to a predetermined slicing condition that approximates geodesic slicing.

can be maintained to perturbation order by a trivial extension of the algebraic condition (8) with $G(\gamma) = 1$, or by solving Eq. (9) with $\dot{K}$ computed from Eq. (70). However, as discussed in the following paragraphs, maintaining this gauge condition can be problematic in numerical evolutions.

Two tests of density evolutions, characterized by the comoving perturbation wavelength in relation to the comoving horizon scale $L_H = 2\sqrt{a}/H_0$, are presented in this section. For perturbations with wavelength $\lambda \gg L_H$, the relative density fluctuations freeze as they are coupled to the expanding background. For $\lambda \ll L_H$, linear perturbations can grow and matter collapses at the rate $\Delta \rho / \rho \propto a \propto t^{2/3}$, as suggested by Eq. (67).

Figure 7 shows the relative errors in γ_{zz} and ρ, and the absolute difference errors in S_z as a function of grid resolution for the super-horizon ($\lambda \gg L_H$) scale perturbations. The initial data is a sine wave perturbation in the potential $\Phi = \Phi_0 \sin(2\pi z/L)$, with $\Phi_0 = 10^{-5}$ and comoving grid size $L = 10^3 L_H$. The errors are evaluated at time $t = 10^6 t_0$ corresponding to $L/L_H \sim 10$ after the z axis expands by a factor of 10^4 in proper length, and scale as $(\Delta t)^2$ and $(\Delta z)^2$. The apparent larger errors in S_z are attributed to plotting the absolute (and not relative) differences between the analytic and numerical solutions, since S_z is a sinusoidal perturbation around zero. Scaling the results by the amplitude of oscillations in S_z (which grow as $a^{3/2} \propto t$), the momentum errors become smaller than those in the density. The results for super-horizon scale perturbations are robust and not especially sensitive to slicing or gauge errors, even though these perturbations are nonlinear in the sense that they couple to the background expansion. However, for perturbations smaller than the horizon scale, the numerical evolutions are susceptible to gauge drift instabilities. In particular, evolu-

tions in which the slicing condition is fixed by some analytic (geodesic or near-geodesic) prescription, i.e. by explicitly enforcing Eqs. (69) and (70), are unstable.

The metric component γ_{zz} is shown in Fig. 8 from five different simulations of sub-horizon scale perturbations ($\lambda \ll L_H$) using 100 zones and the following methods to compute the gauge variables:

Case (A)—Specifying α using Eq. (69) and reconstructing K from the evolved γ_{ij} and K_{ij},

Case (B)—Specifying α and K using Eqs. (69) and (70),

Case (C)—Solving Eq. (9) for α and reconstructing K,

Case (D)—Solving Eq. (9) for α and specifying K using Eq. (70),

Case (E)—Similar to (C), but also implementing a variant of the "K-driver" method [28,29].

The same sinusoidal perturbation form and amplitude are used as in the super-horizon calculations, but with wavelength $\lambda = L_H$ at the initial time $t_0 = 1$. Unlike the super-horizon case, fluctuations at sub-horizon scales can grow to the point where particle trajectories cross, or form shocks in a pressure fluid. An estimate for the time of collapse is derived by setting the amplitude of the density perturbation (67) to unity. This gives

$$t_{coll} = t_0 \left(\frac{x^2}{2\pi^2 \Phi_0} \right)^{3/2}, \tag{71}$$

where the comoving wavelength is parametrized by $\lambda = x L_H$ at $t = t_0$ and, for the prescribed initial data, $t_{coll} \sim 4 \times 10^5 t_0$. To assure the solutions remain in the linear regime for the code tests, the evolutions are terminated at $t = 10^3 t_0$ when $\lambda \sim 10^{-1} L_H$.
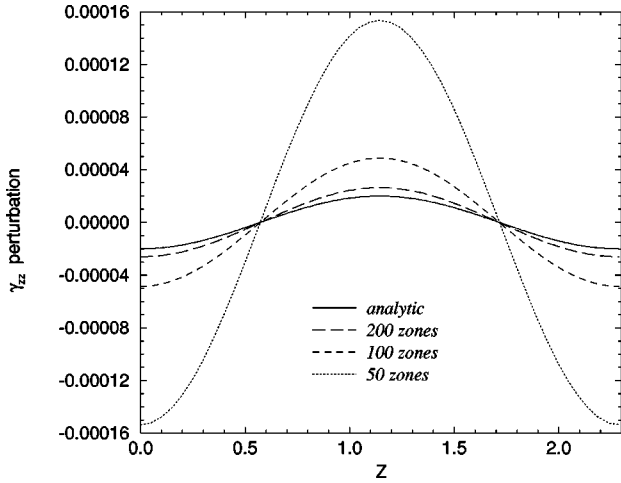
FIG. 9. Sub-horizon scale perturbations in the metric function $(\gamma_{zz} - \bar{\gamma}_{zz})/\bar{\gamma}_{zz}$ at time $t = 10^3 t_0$ for the flat density dominated FLRW model. Results from four different resolution grids are shown for case (D) in Fig. 8 and found to converge quadratically to the analytic solution.

As shown by Fig. 8, the evolutions are unstable for both cases (A) and (B) which specify an analytic form for a lapse function approximating geodesic slicing. When the lapse is allowed to vary during the spacetime evolution, the Eulerian observers can accelerate in response to changes in the local geometry (whether physical or numerical) and the solutions stabilize. Although significant differences can be observed between the analytic and numerical results in Fig. 8, the stable numerical solutions in cases (C) and (D) are convergent, as demonstrated in Fig. 9 where the normalized deviations in γ_{zz} are plotted at three different grid resolutions for the case (D). Figure 10 shows that the errors in γ_{zz} converge to zero quadratically in both time and space. The convergence study is performed on the metric component γ_{zz} since
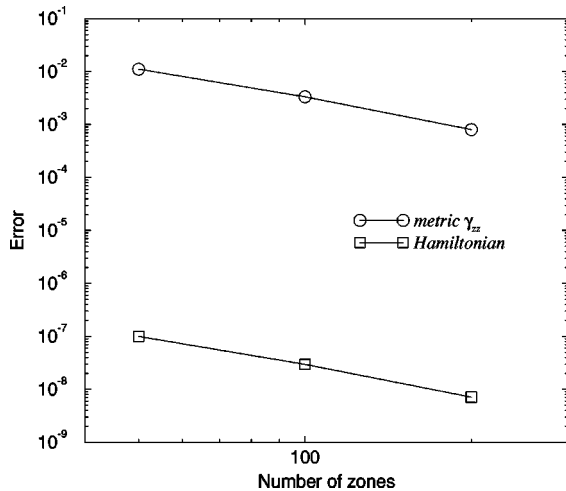

FIG. 10. Convergence study of the errors in γ_{zz}, the metric component most susceptible to the gauge instability. Also shown is the residual of the Hamiltonian constraint. Both curves scale quadratically with resolution to the analytic solution and zero, respectively. The errors are shown for the stable case (D) in Fig. 8.

it displays this gauge drifting behavior most prominently. In fact, γ_{xx}, γ_{yy}, ρ and S_z are not visibly affected and they continue to match the perturbation solution nicely, even when γ_{zz} develops the noise evident in Fig. 8. The Hamiltonian constraint residual (2) is also plotted in Fig. 10 to confirm that errors in the Hamiltonian converge to zero quadratically as expected.

Finally, the case (E) in Fig. 8 is similar to case (C) except Eq. (9) is solved after replacing $\dot{K}$ with

$$\dot{K} = \dot{K}^* - c_0(K - K^*), \tag{72}$$

where K^* is the "target" value defined by Eq. (70). As observed in Fig. 8, this method tends to drive K exponentially to K^* over a characteristic time scale determined by the coefficient c_0. To prevent the solutions from changing too rapidly, which can result in unstable evolutions, c_0 is scaled relative to the Courant timestep as $c_0 = 10^{-3}/\Delta t$. This procedure has proven to be effective in dealing with gauge drifting and numerical errors in simulations of asymptotically flat spacetimes when the maximal slicing condition $K = 0$ is imposed [28,29]. Here, of course, spacetime cannot be globally foliated with $K = 0$ slices since the models are expanding, and one can, in general, expect K to vary significantly over the dynamical time scales. As a result, although the procedure is effective in maintaining the slicing condition (69) and (70), significant cell-to-cell oscillations can result during the evolutions, especially if K is driven to the target too rapidly in comparison to either the dynamical collapse or cosmological expansion time scales.

VI. SUMMARY

A numerical code has been developed as a tool to investigate fully nonlinear behavior in the coupled Einstein field and hydrodynamic matter equations for plane-symmetric cosmological spacetimes. It has been tested against a variety of analytic solutions, including vacuum anisotropically expanding cosmologies, Λ-, dust- and radiation-driven isotropic spacetimes, gravitational waves in flat and anisotropically expanding backgrounds, sub- and super-horizon scale density perturbations in FLRW models, and both Newtonian and relativistic shock tube evolutions to test the shock capturing routines. The code was demonstrated to be second order accurate in both time and space, with errors that scale as $(\Delta t)^2$ and $(\Delta z)^2$ for the smooth field evolutions. Although the evolutions are carried out in an unconstrained manner, the Hamiltonian and momentum constraints are monitered during the evolutions to verify convergence and the degree to which the Einstein equations are satisfied in general nonlinear calculations.

An important improvement over the previous treatments in references [9,10,7,8,3] is the generalization to a nondiagonal metric with arbitrary components restricted only by the Hamiltonian and momentum constraints. This allows for both e_+ and $e_\times$ polarized gravitational waves, and for more general classes of anisotropic and inhomogeneous cosmo-

logical models to be investigated. Additional features include a cosmological constant allowing for de Sitter spacetimes, hydrodynamic ideal fluid sources, a broader selection of slicing conditions, and more general boundary conditions to support periodically identified cosmologies as well as asymptotically flat spacetimes. The code is robust enough to model nonlinear behavior in the gravitational field, as well as in highly dynamic flows of the matter component and their interaction. Results from strong field nonlinear studies will be presented in future papers.

[1] H. Kurki-Suonio, P. Laguna, and R. A. Matzner, Phys. Rev. D **48**, 3611 (1993).

[2] H. Shinkai and K. Maeda, Phys. Rev. D **48**, 3910 (1993).

[3] P. Anninos, J. Centrella, and R. Matzner, Phys. Rev. D **43**, 1825 (1991).

[4] H. Kurki-Suonio, R. A. Matzner, J. Centrella, T. Rothman, and J. R. Wilson, Phys. Rev. D **38**, 1091 (1988).

[5] L. Z. Fang and X. P. Wu, Astrophys. J. **408**, 25 (1993).

[6] R. Tuluie, P. Laguna, and P. Anninos, Astrophys. J. **463**, 15 (1996).

[7] P. Anninos, J. Centrella, and R. Matzner, Phys. Rev. D **39**, 2155 (1989).

[8] P. Anninos, J. Centrella, and R. Matzner, Phys. Rev. D **43**, 1808 (1991).

[9] J. Centrella and J. R. Wilson, Astrophys. J. **273**, 428 (1983).

[10] J. Centrella and J. R. Wilson, Astrophys. J., Suppl. Ser. **54**, 229 (1984).

[11] R. Gowdy, Phys. Rev. Lett. **27**, 826 (1971).

[12] B. Berger, Ann. Phys. (N.Y.) **83**, 458 (1974).

[13] V. Moncrief, Ann. Phys. (N.Y.) **132**, 87 (1981).

[14] V. Moncrief, Phys. Rev. D **28**, 2485 (1983).

[15] B. Berger and V. Moncrief, Phys. Rev. D **48**, 4676 (1993).

[16] R. Arnowitt, S. Deser, and C. W. Misner, in *Gravitation: An Introduction to Current Research*, edited by L. Witten (Wiley, New York, 1962).

[17] D. Bernstein, Ph.D. thesis, University of Illinois at Urbana-Champaign, 1993.

[18] J. R. Wilson, in *Sources of Gravitational Radiation*, edited by L. Smarr (Cambridge University Press, Cambridge, England, 1979).

[19] J. W. York, in *Sources of Gravitational Radiation*, edited by L. Smarr (Cambridge University Press, Cambridge, England, 1979).

[20] C. Evans, Ph.D. thesis, University of Texas at Austin, 1984.

[21] Ya. B. Zel'dovich, Astron. Astrophys. **5**, 84 (1970).

[22] P. J. Roache, *Computational Fluid Dynamics* (Hermosa, Albuquerque, New Mexico, 1972).

[23] J. F. Hawley, L. L. Smarr, and J. R. Wilson, Astrophys. J., Suppl. Ser. **55**, 211 (1984).

[24] B. van Leer, J. Comput. Phys. **23**, 276 (1977).

[25] J. M. Stone and M. L. Norman, Astrophys. J., Suppl. Ser. **80**, 753 (1992).

[26] E. Kasner, Am. J. Math. **43**, 217 (1921).

[27] V. Mukhanov, H. Feldman, and R. Brandenberger, Phys. Rep. **215**, 203 (1992).

[28] K. Eppley, in *Sources of Gravitational Radiation*, edited by L. Smarr (Cambridge University Press, Cambridge, England, 1979).

[29] J. Balakrishna, G. Daues, E. Seidel, W. M. Suen, M. Tobias, and E. Wang, Class. Quantum Grav. **13**, L135 (1996).